

Simulation of Channeling and Radiation of 855 MeV Electrons and Positrons in a Small-Amplitude Short-Period Bent Crystal

Andrei V. Korol ^{a,1} Victor G. Bezchastnov,^{2,3}
Gennady B. Sushko,¹ and Andrey V. Solov'yov¹

¹*MBN Research Center, Altenhöferallee 3, 60438 Frankfurt am Main, Germany*

²*A.F. Ioffe Physical-Technical Institute,
Politechnicheskaya Str. 26, 194021 St. Petersburg, Russia*

³*Peter the Great St. Petersburg Polytechnic University,
Politechnicheskaya 29, 195251 St. Petersburg, Russia.*

Channeling and radiation are studied for the relativistic electrons and positrons passing through a Si crystal periodically bent with a small amplitude and a short period. Comprehensive analysis of the channeling process for various bending amplitudes is presented on the grounds of numerical simulations. The features of the channeling are highlighted and elucidated within an analytically developed continuous potential approximation. The radiation spectra are computed and discussed.

PACS numbers: 02.70.Ns, 41.60.-m, 61.85.+p, 83.10.Rs

^a E-mail: korol@mbnexplorer.com

I. INTRODUCTION

Channeling of the charged projectiles in crystals establishes a field of research important both with respect to the fundamental theoretical studies as well as to the ongoing experiments (see, e.g., the monograph [1] and the references therein). Starting from the first theoretical predictions by Lindhard [2], the channeling is known to occur when the projectiles move in the crystals preferably along the crystalline planes or axes. This phenomenon opens a possibility to manipulate the beams of projectiles, in particular by deflecting them in bent crystals.

Of particular interest for the theory and applications is the radiation produced by the channeling projectiles. The radiation spectra display distinct lines related to the inter-planar oscillations or axial rotations of the particles involved into the planar or axial channeling, respectively, in contrast to the bremsstrahlung-type spectra produced by the non-channeling projectiles. In periodically bent crystals, the channeling radiation exhibit additional *undulator lines* as a result of modulation of the transverse velocity of the moving particles by the bent crystalline structure. The positions of the undulator lines depend on the bending period and the projectile energies and thereby can be tuned in an experiment. Theoretically, a crystalline undulator has been suggested [3, 4] as a source of the monochromatic radiation of sub-MeV to MeV energies, and different experiments have been being performed to produce and detect the undulator radiation.

The original concept of the crystalline undulator assumes the projectiles to move through the crystal following the periodically bent crystalline planes or axes. For such motions, the undulator modulation frequencies are smaller than the frequencies of the channeling oscillations or rotations providing the undulator spectral lines to arise at the energies below the energies of the channeling lines. Recently, channeling has been studied for periodically bent crystals with the bending period shorter than the period of channeling oscillations in the straight crystal [5, 6]. The emergent radiation was shown to display spectral lines at the energies exceeding the energies of the channeling peaks. The corresponding theoretical simulations have been performed for the electron and positron channeling in the silicon crystals with the (110)-planes bent according to the shapes

$$\delta(z) = a \cos(2\pi z/\lambda_u), \quad (1)$$

where z is a coordinate along the planes in the straight crystal, whereas a and λ_u are

the bending amplitude and period, respectively. The simulations have also assumed the amplitude a to be substantially smaller than the inter-planner distance d in the straight crystal. In contrast to the channeling in conventional crystalline undulator, for the newly proposed crystalline structures the channeling projectiles do not follow the short-period bent planes. The positrons move bouncing between the bent planes, whereas the electrons move preferable through the small-amplitude “waves” of the bent structures. Yet the motion of the projectiles acquires a short-period modulation resulting from the bending and explicitly seen in the theoretically simulated trajectories [6]. These modulations are of a regular jitter-type and responsible for producing the high-energy monochromatic radiation. Interestingly, a similar radiative mechanism has recently been studied with respect to the radiation produced by relativistic particles in interstellar environments with turbulent small-scale fluctuations of the magnetic field [7, 8].

It requires, in our view, some future clarifications on whether the jitter-type channeling motions in crystals provide observable properties (in particular for the radiation detected) inherent to the conventional undulator. Within the current studies, we adopt the term *small-amplitude short-period* (SASP) to designate the bent crystalline structures suggested in Ref. [5]. Important is that, the SASP bent crystals can be regarded as possible efficient sources of tunable monochromatic hard-energy radiation and therefore are of immediate interest for applications and further theoretical studies.

Since introducing the SASP bent crystals [5], several theoretical and experimental studies have already been performed on the new regime of channeling and the radiation produced [6, 9]. However, further efforts are certainly required for more detailed investigations on statistical properties of channeling as well as on computing the radiation spectra for a variety of conditions including different bending parameters, lengths of the crystalline samples, beam energies and angular apertures for detecting the radiation. The focus of the present paper is on the theoretical simulations for the electrons and positrons with the energies of 855 MeV that are the beam energies achievable in experiments at Mainz Microtron Facility [9, 24].

As in a number of our recent studies, three-dimensional simulations of the propagation of ultra-relativistic projectiles through the crystal are performed by using the MBN EXPLORER package [10, 11]. This package was originally developed as a universal numerical tool to study structure and dynamics on the spatial scales from nanometers and above for a wide

range of complex atomic and molecular systems. In order to address the channeling phenomena, an additional module has been incorporated into the MBN EXPLORER to compute the motion for relativistic projectiles along with dynamical simulations of the propagation environments, including the crystalline structures, in the course of projectile's motion [12]. These computations advance to account for the interaction of the projectiles with the separate atoms of the environments, whereas a variety of interatomic potentials implemented in MBN EXPLORER support rigorous simulations of various media. The developed software package can be regarded as a powerful numerical tool to uncover the dynamics of relativistic projectiles in crystals, amorphous bodies, as well as in biological environments. Its efficiency and reliability has already been benchmarked for the channeling in crystals [6, 12–16]. The calculated with the MBN EXPLORER relativistic motion, represented by the projectile's coordinates and velocities at the instances of the propagation time, is used as the input data to compute the spectral and/or the spectral-angular distributions of the emitted radiation. A module for calculating the radiation emergent from the channeling is included into the latest version of MBN EXPLORER [11].

II. THEORETICAL FRAMEWORK

We consider the motion of the projectiles through the crystal as being governed by the laws of classical relativistic dynamics:

$$\partial\mathbf{r}/\partial t = \mathbf{v}, \quad \partial\mathbf{p}/\partial t = -q \partial U/\partial\mathbf{r}, \quad (2)$$

where $\mathbf{r}(t)$ is the coordinate, $\mathbf{v}(t)$ is the velocity and $\mathbf{p}(t) = m\gamma\mathbf{v}(t)$ is the momentum of the particle at the propagation time t , $\gamma = (1 - v^2/c^2)^{-1/2} = \varepsilon/mc^2$ is the relativistic Lorentz-factor, ε and m are the energy and the rest mass of the particle, respectively, and c is the speed of light. The driving force, sensitive to the charge q of the projectile, stems from an electrostatic potential $U = U(\mathbf{r})$ for the particle-crystal interaction. MBN EXPLORER allows for computing the latter potential from the interactions of the projectile with the individual atoms,

$$U(\mathbf{r}) = \sum_j U_{\text{at}}(|\mathbf{r} - \mathbf{R}_j|). \quad (3)$$

The spacial locations \mathbf{R}_j of the atoms are selected according to the crystalline structures of the interest (including the effect of thermal fluctuations). The atomic potentials U_{at} in

our simulations are evaluated within the Moliere approximation [17]. A rapid decrease of these potentials with increasing the distances from the atoms allows to truncate the sum (3) in practical calculations. MBN EXPLORER provides an option to restrict the atoms contributing to the interaction $U(\mathbf{r})$ to those located inside a cut-off sphere around the coordinate \mathbf{r} , as well as invokes an efficient linked-cell algorithm to search for the atoms inside this sphere.

A particular feature of MBN EXPLORER is simulating the environment “on the fly” i.e. in the course of computing the motion of the projectiles. For channeling, the crystalline lattice is simulated inside a box surrounding the position of the projectile and the simulation box shifts accordingly to the motion of the projectile. The coordinate frame for the simulations has the z -axis along the incoming beam and parallel to the crystalline planes responsible for the channeling, whereas the y axis is set perpendicular to these planes. In order to exclude an accidental axial channeling, the z -axis should avoid major crystallographic directions. For channeling along the (110) planes, we opted to define the z -axis by a direction $\langle -nm \rangle$ with $n \gg m \sim 1$.

The simulation box is filled by the crystalline lattice with the nodes $\mathbf{R}_j = \mathbf{R}_j^{(0)} + \mathbf{\Delta}_j$, selected with account for the thermal displacements $\mathbf{\Delta}_j$ of the atomic nuclei with respect to the equilibrium positions $\mathbf{R}_j^{(0)}$. The equilibrium nodes correspond to the Bravais cells for the crystal, whereas the Cartesian components Δ_{jk} ($k = x, y, z$) of the thermal displacements are selected randomly according to the normal distribution

$$w(\Delta_{jk}) = \frac{1}{\sqrt{2\pi u_T^2}} \exp\left(-\frac{\Delta_{jk}^2}{2u_T^2}\right). \quad (4)$$

The values of the amplitude u_T of the thermal vibrations are well-known for various crystals and can be found in Ref. [18]. For the silicon crystals at room temperature we use the value $u_T = 0.075 \text{ \AA}$.

The equations (2) are numerically integrated forth from $t = 0$ when the particle enters the crystal at $z = 0$. The initial values x_0 and y_0 for the transverse coordinates are selected randomly from an entrance domain where the beam can be guided by the crystalline planes to get into the inside of the crystal. The size of this domain is taken between $2d$ and $5d$ in the x -direction and between d and $3d$ in the y -direction, where d is the inter-planer separation for the crystal. The initial velocity $\mathbf{v}_0 = (v_{0x}, v_{0y}, v_{0z})$ has the value determined by the beam energy and is predominantly oriented in the z -direction, i.e. the values v_{0x} and

v_{0y} are small compared to the value $v_{0z} \approx c$. The non-vanishing v_{0x} and v_{0y} can be adjusted to account for the beam emittance. The data presented below in Sects. III A and III B are obtained for the zero emittance, $v_{0x} = v_{0y} = 0$.

When computing the motion of the projectile through the crystal with MBN EXPLORER, an efficient algorithm of “dynamic simulation box” [12] is used as follows. Inside a simulation box, the particle interacts with the atoms of the cutoff sphere. As the particle moves, the sphere shifts and at some point meets an edge of the box. Once this happens, a new simulation box is introduced being centered at the current position of the projectile. The new box is then filled with the crystalline lattice such that the nodes inside the intersection of the old and the new simulation boxes remain unchanged i.e. not being simulated anew with including the effect of the thermal vibrations. This allows to avoid a spurious change in the driving force as well as reduces numerical efforts in simulating the crystalline environment in the course of the projectile’s motion.

The above described numerical propagation procedure terminates when the z -coordinate of the projectile approaches the thickness L of the crystal under study. To simulate a periodically bent crystal, the y -coordinates for each lattice node $\mathbf{R}_j = (X_j, Y_j, Z_j)$ are obtained from these for the straight crystal by the transformation $Y_j \rightarrow Y_j + \delta(Z_j)$ with $\delta(Z_j)$ being determined by the bending profile (1).

Employing the Monte-Carlo technique for sampling the incoming projectiles as well as for accounting for the thermal fluctuations of the crystalline lattice yields a statistical ensemble of trajectories simulated with MBN EXPLORER. The trajectories then can be used for computing the radiation from the projectiles passing through the crystal. The energy emitted per unit frequency ω within the cone $\theta \leq \theta_{\max}$ along the z axis is computed as follows

$$\frac{dE(\theta \leq \theta_{\max})}{d\omega} = \frac{1}{N_0} \sum_{n=1}^{N_0} \int_0^{2\pi} d\phi \int_0^{\theta_{\max}} \theta d\theta \frac{d^2 E_n}{d\omega d\Omega}, \quad (5)$$

where the sum is carried over the simulated trajectories of the total number N_0 , Ω is the solid angle corresponding to the emission angles θ and ϕ , and $d^2 E_n/d\omega d\Omega$ is the energy per unit frequency and unit solid angle emitted by the projectile moving along the n th trajectory. The general equation (5) accounts for contributions of *all the segments* of simulated trajectories i.e. the segments of the channeling motion as well as the segments of motion out of the channeling regime.

The radiation emitted by the individual projectiles is computed within the quasi-classical approach developed by Baier and Katkov. For the details of the formalism as well as various applications to radiative processes we refer to the monograph [19] (we also mention Appendix A in Ref. [20] where a number of intermediate steps of the formalism are evaluated explicitly). It is to be pointed out that, along with the classical description of the motion of projectiles, the formalism includes the effect of quantum radiative recoil i.e. it accounts for the change of the projectile energy due to the photon emission. The impact of the recoil on the radiation is governed by the ratio $\hbar\omega/\varepsilon$, and the limit $\hbar\omega/\varepsilon \rightarrow 0$ corresponds to purely classical description of the radiative process. For channeling, the classical framework is found to be adequate for calculations of the radiation produced in straight, bent and periodically bent crystals by the electrons and positrons with the sub-GeV beam energies (see, e.g, the monograph [1] and the references therein). For higher beam energies, the quantum recoil can become important, and has recently be shown [6] to significantly influence the radiation produced in SASP bent crystals by the multi-GeV electrons and positrons.

To compute the spectral intensity of the radiation produced by the particle moving along the trajectory $\mathbf{r} = \mathbf{r}(t)$ in the crystal of the thickness L , we use the equation [1, 12]:

$$\frac{d^2E}{\hbar d\omega d\Omega} = \alpha q^2 \omega^2 \frac{(1+u)(1+w)}{4\pi^2} \left[\frac{w |I_z|^2}{\gamma^2(1+w)} + |\sin\phi I_x - \cos\phi I_y|^2 + |\theta I_z - \cos\phi I_x - \sin\phi I_y|^2 \right], \quad (6)$$

where α is the fine structure constant, q is the charge of the projectile in units of the elementary charge, $u = \hbar\omega/(\varepsilon - \hbar\omega)$ and $w = u^2/(1+u)$. The quantities $I_{x,y,z}$ involve the integrals with the phase functions,

$$I_z = \int_0^\tau dt e^{i\omega'\Phi(t)} - \frac{i}{\omega'} \left(\frac{e^{i\omega'\Phi(0)}}{D(0)} - \frac{e^{i\omega'\Phi(\tau)}}{D(\tau)} \right), \quad (7)$$

$$I_{x,y} = \int_0^\tau dt \frac{v_{x,y}(t)}{c} e^{i\omega'\Phi(t)} - \frac{i}{\omega'} \left(\frac{v_{x,y}(0)}{c} \frac{e^{i\omega'\Phi(0)}}{D(0)} - \frac{v_{x,y}(\tau)}{c} \frac{e^{i\omega'\Phi(\tau)}}{D(\tau)} \right),$$

where $\tau = L/c$ is the time of flight through the crystal, $D(t) = 1 - \mathbf{n} \cdot \mathbf{v}(t)/c$, $\Phi(t) = t - \mathbf{n} \cdot \mathbf{r}(t)/c$, \mathbf{n} is the unit vector in the emission direction, and $\omega' = (1+u)\omega$. The quantum radiative recoil is accounted for by the parameter u which vanishes in the classical limit.

III. CHANNELING AND RADIATION FOR 855 MEV ELECTRONS AND POSITRONS

Within the above described theoretical framework and by exploiting the MBN EXPLORER package, the trajectories and radiation spectra have been simulated for the $\varepsilon = 855$ MeV electrons and positrons. The projectiles were selected as incoming along the (110) crystallographic planes in a straight silicon crystal, and the SASP bent crystalline profiles were introduced according to Eq. (1).

The amplitude and period of bending were varied within the intervals $a = 0.05 \dots 0.95$ Å (providing a to be smaller than the distance $d = 1.92$ Å between the (110) planes in the straight Si crystal) and $\lambda_u = 100 \dots 2500$ nm. These ranges include the values used in the recent theoretical [5, 6] and experimental [9] studies on the channeling and radiation for SASP bending. The results we have obtained reveal a variety of peculiar features of the channeling in SASP bent Si(110). A qualitative analysis of these results is presented in Section III A.

The calculated emission spectra cover a wide range of the photon energies, from $\lesssim 1$ MeV up to 40 MeV. The calculations were performed for the crystal thicknesses 12, 25, 75 and 150 micron measured along the beam direction. The integration over the emission angle θ was carried out for two particular detector apertures determined by the values $\theta_{\max} = 0.21$ and 4 mrad. The first value is close to one used in the experiments with the 855 MeV electron beam at Mainz Microtron facility [9, 21–24], and is much smaller than the natural emission angle for the beam energy, $\gamma^{-1} \approx 0.6$ mrad. Therefore, the corresponding spectra refer to a nearly forward emission. The second angle value, in contrast, significantly exceeds the value γ^{-1} providing the emission cone with $\theta \leq \theta_{\max}$ to collect almost all the radiation from the relativistic projectiles. The latter situation corresponds to the conditions at the experimental setup at SLAC [25]. The discussion of the calculated emission spectra is given in Section III B.

A. Statistical Properties of Channeling

For each type of the projectiles and different sets of the bending amplitudes and periods (including the case of the straight crystal with $a = 0$), the numbers N_0 of the simulated

trajectories were sufficiently large (between 4000 and 7000) thus enabling a reliable statistical quantification of the channeling process. Below we define and describe the quantities obtained.

A randomization of the “entrance conditions” for the projectiles (in particular sampling the entrance locations as explained in Sect. II) makes the different projectiles to encounter differently scattering with the crystalline atoms upon entering the crystal. As a result, not all the simulated projectiles start moving through the crystal in a channeling mode. A commonly used parameter to quantify the latter property is *acceptance* defined as the ratio $\mathcal{A} = N_{\text{acc}}/N_0$ of the number N_{acc} of particles captured into the channeling mode once entering the crystal (the accepted particles) to the number N_0 of the incident particles. The non-accepted particles experience over-barrier motion unrestricted in the inter-planar directions.

It is order to notice that different theoretical approaches to the interaction of the projectiles with the crystalline environments are also different in criteria distinguishing between the channeling and the over-barrier motions. For example, the continuous potential approximation [2] decouples the transverse (inter-planar) and longitudinal motions of the projectiles. As a result, it is straightforward to distinguish the channeling projectiles as those with transverse energies not exceeding the height of the inter-planar potential barrier. In our simulations, the projectiles interact, as in reality, with the individual atoms of the crystal. The inter-planar potential experienced by the projectiles vary rapidly in the course of their motion and couples the transverse and longitudinal degrees of freedom. Therefore, another criteria are required to select the channeling episodes in the projectile’s motion. We assume the channeling to occur when a projectile, while moving in the same channel, changes the sign of the transverse velocity v_y at least two times [26]. The latter criteria have also to be supplemented by geometrical definitions of the crystalline channels. Here, we refer to the straight crystals where the positron channels are the volume areas restricted by the neighboring (110) planes, whereas the electron channels are the areas between the corresponding neighboring mid-planes. For SASP bent crystals, the simulations show that, at small values of the bending amplitude, the channeling occur in the above defined channels for the straight crystal. We will refer to such situation as to the “conventional” channeling. With the amplitudes increasing above some values, the positrons tend to channel in the electron channels for the straight crystal, and vice versa, the electrons become channeling

in the positron channels. The latter situation will be regarded as the “complementary” channeling. We will provide below a quantification for both channeling regimes.

For an accepted projectile, the channeling episode lasts until an event of de-channeling when the projectile leaves the channel. The de-channeling events occur mostly as cumulative outcomes of multiple collisions of the projectiles with the crystalline constituents. Also, a rare large-angle scattering collision can lead to de-channeling. De-channeling of the accepted particles is conveniently quantified by the *penetration depth* L_{p1} evaluated as the mean longitudinal extension of the primary channeling segments of the trajectories. The latter segments are those that start at the crystalline entrance and end at the first de-channeling event experienced by the particle inside the crystal [12]. The penetration depth can be related to a commonly used de-channeling length L_d . Within the framework of the diffusion theory of de-channeling (see, e.g., Ref. [27]), the fraction of the channeling particles at large distances z from the entrance decays exponentially, $\propto \exp(-z/L_d)$, with increasing z [28]. Assuming the decay law to be applicable for all z , the penetration depth can be evaluated as the integral $L_{p1} = \int_0^L (z/L_d) \exp(-z/L_d) dz$ and appears to be smaller than L_d for the finite lengths L of the crystalline samples. For sufficiently long crystals, $L \gg L_d$, the penetration depth approaches the de-channeling length, $L_{p1} \rightarrow L_d$.

Random scattering of the projectiles on the crystalline constituents can also result in a *re-channeling* process of capturing the over-barrier particles into the channeling mode of motion. This process is quantified by the *re-channeling length*, L_{rech} , defined as an average distance along the crystal between the trajectory points corresponding to the successive events of de-channeling and re-channeling. We notice that, the re-channeling events are more frequent (and, correspondingly, the re-channeling lengths are shorter) for the negatively charged projectiles than these for the positively charged ones. For a qualitative explanation of this feature we refer to Ref. [26].

In a sufficiently long crystal, the projectiles can experience de-channeling and re-channeling several times in the course of propagation. These multiple events are accounted for by an additional pair of lengths, the penetration length L_{p2} and the total channeling length L_{ch} that characterize the channeling process in the whole crystal. The depth L_{p2} is the average extension calculated with respect to *all* channeling segments in the trajectories, i.e. not only with respect to the segments that start from the crystalline entrance and are used to evaluate L_{p1} but also including the segments that appear inside the crystal due

to the re-channeling events followed by de-channeling. The total channeling length L_{ch} is computed as the average length with respect to all channeling segments per trajectory.

As a result of re-channeling, the projectiles become captured into the channels when possess, statistically, the incident angles of the values smaller than the Lindhard's critical angle values Θ_L [2]. Therefore, for sufficiently thick crystals, the lengths $L_{\text{p}2}$ provide the estimates of the de-channeling lengths L_d for the beams with the emittance values $\approx \Theta_L$.

The above described statistical quantities have been calculated from the simulations on the channeling for the 855 MeV electrons and positrons in the straight and SASP bent Si(110) crystals of the thickness $L = 150$ micron. The value of the bending period has been fixed at $\lambda_u = 400$ nm, and different values of the bending amplitude a have been selected. The results on the acceptance and characteristic lengths are presented in Table I. All the data refer to the zero emittance beams. Statistical uncertainties due to the finite (but sufficiently big) numbers of the simulated trajectories correspond to the confidence probability value of 0.999.

Let us first discuss the channeling properties for small to moderate values of the bending amplitude, $a \leq 0.6$ Å. Comparing the values of $L_{\text{p}1}$, $L_{\text{p}2}$ and L_{ch} for the electrons with these for the positrons reveals that, all three lengths for the positrons noticeably exceed, up to the order of magnitude, the corresponding lengths for the electrons. The latter is not surprising given that fact that the channels optimally guiding the particles through the crystal are different for the positrons and electrons due to the different character of the the particle-crystal interactions. As the interactions with the crystalline atoms are repulsive for the positrons and attractive for the electrons, the channels guide these particles to move in the domains with low and high content of the crystalline atoms, respectively. In course of the projectile's motion, the electrons experience scattering on the atoms more frequent as the positrons. As a result, for the electrons the de-channeling process develops faster and results in shorter penetration and channeling lengths than for the positrons. The penetration lengths $L_{\text{p}1}$ and $L_{\text{p}1}$ for the electrons appear to be close to each other within the statistical uncertainties, for almost all the bending profiles studied in Table I, as well as to be much shorter than the thickness $L = 150$ micron for the simulated crystalline sample. Therefore, either of these lengths can be regarded as the de-channeling length for the electrons. For the positrons, two penetration scales, $L_{\text{p}1}$ and $L_{\text{p}2}$, appear to be different, with the values $L_{\text{p}2}$ being systematically smaller than the values $L_{\text{p}1}$. For small bending amplitudes, the

TABLE I. Acceptance \mathcal{A} , penetration depths $L_{p1,2}$, total channeling length L_{ch} and re-channeling length L_{rech} for 855 MeV electrons and positrons channeling in $L = 150 \mu\text{m}$ thick straight and SASP bent Si(110). The bending period is $\lambda_u = 400 \text{ nm}$, and the different values of the bending amplitude a are examined. Two sets of statistical quantities given in the upper and bottom lines for $a = 0.7, 0.8$ and 0.9 \AA are deduced from the “conventional” and “complementary” trajectories, respectively (for the detailed explanations see the text).

electron channeling					
$a \text{ (\AA)}$	\mathcal{A}	$L_{p1} \text{ (\mu m)}$	$L_{p2} \text{ (\mu m)}$	$L_{ch} \text{ (\mu m)}$	$L_{rech} \text{ (\mu m)}$
0.00	0.64	11.89 ± 0.49	11.19 ± 0.19	42.10 ± 1.21	24.12 ± 0.76
0.05	0.61	9.05 ± 0.43	8.98 ± 0.17	39.35 ± 1.49	21.44 ± 0.87
0.10	0.54	6.37 ± 0.32	6.60 ± 0.10	34.46 ± 1.40	19.20 ± 0.83
0.15	0.48	5.45 ± 0.30	5.69 ± 0.09	30.78 ± 1.39	19.39 ± 0.89
0.20	0.48	5.77 ± 0.33	5.71 ± 0.10	26.38 ± 1.16	23.43 ± 1.01
0.25	0.50	6.79 ± 0.43	6.40 ± 0.14	25.87 ± 1.17	26.38 ± 1.15
0.30	0.56	8.20 ± 0.43	7.59 ± 0.17	26.07 ± 1.02	30.31 ± 1.12
0.40	0.70	10.74 ± 0.57	10.04 ± 0.26	30.20 ± 1.28	32.89 ± 1.40
0.50	0.73	11.00 ± 0.57	10.01 ± 0.26	31.37 ± 1.43	30.22 ± 1.40
0.60	0.78	10.63 ± 0.55	10.23 ± 0.27	32.89 ± 1.61	29.22 ± 1.49
0.70	0.81	8.83 ± 0.47	9.09 ± 0.23	27.70 ± 1.43	31.30 ± 1.62
	0.64	5.25 ± 0.25	5.70 ± 0.11	20.12 ± 1.10	29.51 ± 1.53
0.80	0.71	4.71 ± 0.23	5.44 ± 0.10	21.78 ± 1.08	26.33 ± 1.26
	0.79	7.06 ± 0.33	7.70 ± 0.16	26.03 ± 1.05	29.21 ± 1.40
0.90	0.36	2.16 ± 0.10	2.63 ± 0.03	13.55 ± 0.67	22.77 ± 1.04
	0.72	8.10 ± 0.17	7.86 ± 0.17	27.18 ± 1.34	28.84 ± 1.30
positron channeling					
$a \text{ (\AA)}$	\mathcal{A}	$L_{p1} \text{ (\mu m)}$	$L_{p2} \text{ (\mu m)}$	$L_{ch} \text{ (\mu m)}$	$L_{rech} \text{ (\mu m)}$
0.00	0.95	131.45 ± 3.11	100.03 ± 4.11	131.19 ± 3.02	29.75 ± 4.20
0.10	0.92	124.39 ± 2.78	84.45 ± 3.09	122.59 ± 2.66	29.38 ± 2.49
0.20	0.89	115.38 ± 2.99	65.04 ± 2.62	111.97 ± 2.81	27.48 ± 1.87
0.30	0.88	99.46 ± 3.44	48.34 ± 2.25	100.63 ± 3.04	25.82 ± 1.59
0.40	0.86	84.68 ± 4.05	36.65 ± 2.12	87.50 ± 3.53	26.23 ± 1.64
0.50	0.84	63.85 ± 3.94	23.44 ± 1.47	70.68 ± 3.33	24.21 ± 1.30
0.60	0.80	41.70 ± 3.23	13.76 ± 0.84	52.96 ± 2.64	22.26 ± 1.00
0.70	0.74	13.41 ± 1.56	6.23 ± 0.29	31.53 ± 1.58	20.22 ± 0.94
	0.50	6.12 ± 0.34	3.44 ± 0.09	22.17 ± 1.03	16.32 ± 0.75
0.80	0.58	3.60 ± 0.19	3.60 ± 0.04	20.77 ± 0.77	19.17 ± 0.72
	0.66	9.20 ± 0.43	6.10 ± 0.15	27.75 ± 1.01	21.66 ± 0.84
0.90	0.29	2.01 ± 0.09	2.78 ± 0.02	17.74 ± 0.77	18.40 ± 0.73
	0.80	15.94 ± 0.76	12.50 ± 0.34	40.68 ± 1.56	27.26 ± 1.14

positron penetration scales are not much shorter than the thickness of the crystals studied, and therefore none of these scales are close to the de-channeling lengths. Estimating the positron de-channeling length on the grounds of the continuous potential approximation (Eq. (1.50) of Ref. [27]) yields for the straight Si(110) crystal the length $L_d \approx 570$ micron essentially longer than the crystalline thickness. Therefore, the values for the positron penetration scales L_{p1} presented in Table I can be considered only as the lower bounds for the positron de-channeling length.

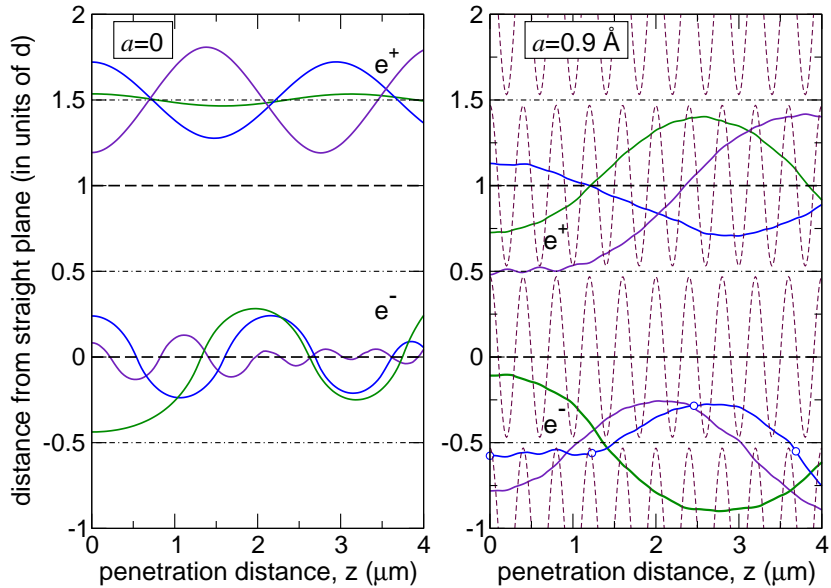


FIG. 1. Channeling trajectories for the electrons (e^-) and positrons (e^+) in the straight (left plot) and periodically bent (right plot) Si(110). Thick dashed lines correspond to the straight (110)-planes, chained lines mark the centerlines between the planes. Thin dashed lines in the right plot show the profiles of the planes bent with $a = 0.9 \text{ \AA}$ and $\lambda_u = 400 \text{ nm}$. The trajectories shown in the left and right plot can be regarded as “conventional” and “complementary”, respectively. Notice the shift $d/2$ (d is the inter-planar distance) between the equilibrium positions for the transverse oscillations of the projectiles in the left- and right-plot trajectories.

A close look at the trajectories simulated for various bending amplitudes reveals the channeling segments in the trajectories to be of two different kinds that can be called “conventional” and “complementary”. The fraction of “complementary” segments in the simulated trajectories is small and the corresponding channeling lengths are very short for the bending amplitudes $a \leq 0.2 \text{ \AA}$. With increasing a the latter fraction extends and dominates

over the “conventional” fraction as the amplitude approaches the value $d/2$ with d being the inter-planar distance in straight Si(110). The two kinds of the channeling trajectory segments yield essentially different values for the statistical quantities. In Table I, the quantities deduced from the “complementary” segments are given in the lower lines for $a = 0.7, 0.8$ and 0.9 \AA . All the other quantities in the table are computed from the “conventional” segments.

To explain the introduced terminology and to illustrate the dramatic change in the channeling processes for the projectiles with increasing a we refer to Fig. 1. The left plot in the figure shows the channeling segments of the trajectories in the straight crystal. There, the projectiles exhibit the “conventional” channeling where the electrons oscillate around the crystalline planes whereas the positrons oscillate around the centerlines between the planes. In the bent crystal studied in the right plot for $a = 0.9 \text{ \AA}$ we encounter the “conventional” channeling trajectory segments. There, the transverse oscillations appear around the equilibrium positions that are shifted in the inter-planar direction by the distance $d/2$ with respect to the equilibrium positions in the straight crystal. In other words, the equilibrium positions for the transverse oscillations of the electrons and the positrons are reversed in the “conventional” and “complementary” trajectory segments. The fraction of “complementary” segments in the simulated trajectories, being negligible for $a \leq 0.2 \text{ \AA}$, increases with increasing bending amplitude and for $a \approx d/2$ almost all the channeling segments become “complementary”.

The data presented in Table I demonstrate that, the channeling lengths $L_{p1,2}$ and L_{ch} change with varying the bending period a for the electrons and for the positrons in essentially different manner. To illustrate the difference, Fig. 2 shows the primary penetration lengths L_{p1} as functions of a for the electrons (left plot) and the positrons (right plot). The length computed from the “conventional” trajectory segments (solid curves in the figure) vary monotonously with a for the positrons and exhibits pronounced local minimum and maximum in the range $a \leq 0.6 \text{ \AA}$ for the electrons. The penetration lengths deduced from the “complementary” segments increase with increasing a (dashed curves in the figure) being smaller than the “conventional” lengths unless a approaches the values $\approx 0.75 \text{ \AA}$ for both types of the projectiles. For larger bending amplitudes the “complementary” channeling segments become on average longer than the “conventional” segments that display the values for the penetration lengths close to each other for the electrons and positrons.

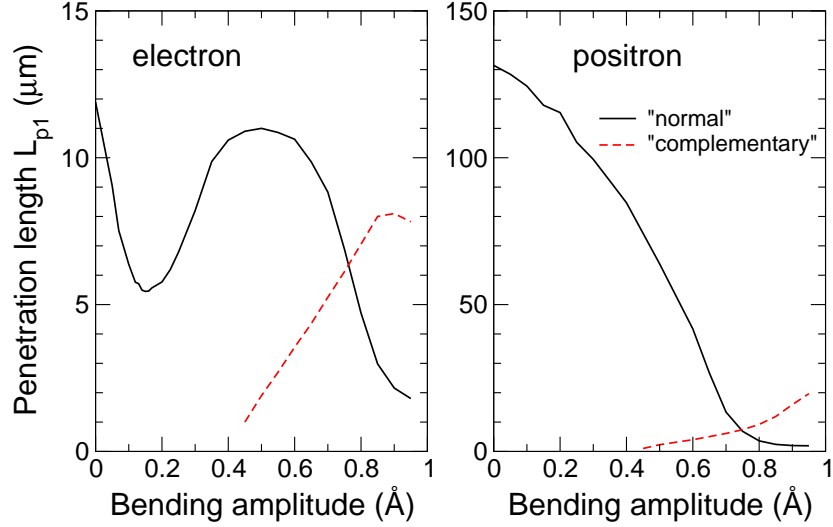


FIG. 2. Penetration length L_{p1} versus bending amplitude for the 855 MeV electrons (left plot) and positrons (right plot) in SASP bent Si(110). The bending period is fixed at 400 nm. The solid and dashed curves represent the dependencies calculated from the “conventional” and “complementary” channeling trajectory segments, respectively. See also explanations in the text.

The origin of the peculiarities described above are the changes in the particle-crystal interactions with changing the bending amplitudes. As already discussed, the positrons and electrons tend to channel in the domains with low and high content of the crystalline constituents, respectively. In order to highlight how these domains change with changing the bending amplitude, a continuous inter-planar potential experienced by the moving projectiles can be considered. To calculate this potential for a periodically bent crystal we used the approach described in A. The non-periodic part of the emerging potential, Eq. (A1), is evaluated by using the Molière atomic potentials. This part is presented in Fig. 3 for the electrons (left plot) and positrons (right plot), for different values of the bending amplitudes (given in \AA near the curves). Fig. 4 shows the corresponding volume densities of the crystalline electrons and nuclei.

In Fig. 3, the potential curves labeled with “0” correspond to the straight crystal. For small amplitude values, $a \leq 0.2 \text{\AA}$, the major changes in the potentials with increasing a are decreasing potential barriers and, for the electrons, a broadening potential well. As the a values approach $0.4 \dots 0.6 \text{\AA}$, the volume density of atoms becomes more friable and leads to flattening of the potential in the vicinity of the potential minimum for the electrons and of the potential maximum for the positrons. For larger amplitude values, the potentials change in a

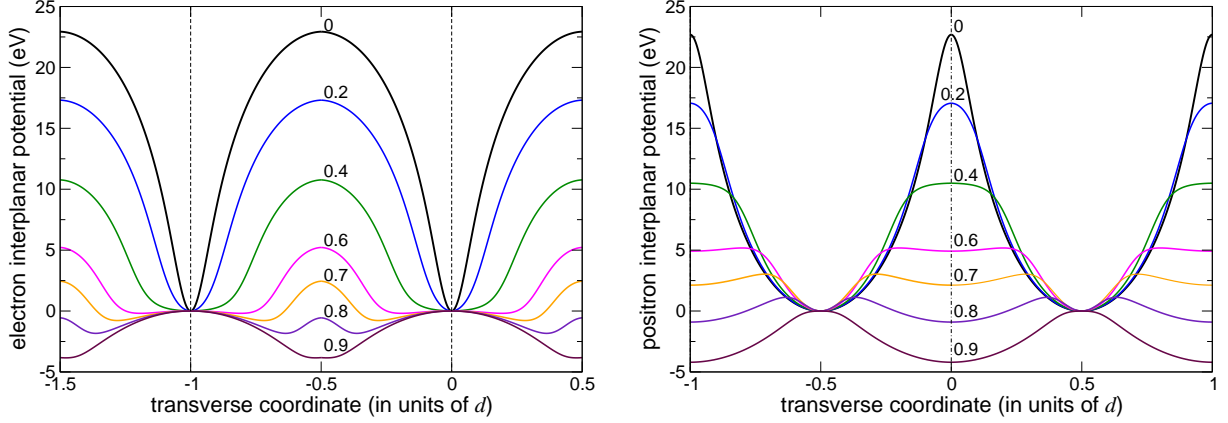


FIG. 3. Continuous inter-planar potentials for the electrons (left plot) and positrons (right plot) for different values of the bending amplitude indicated in \AA near the curves ($a = 0$ corresponds to the straight crystal). The potentials shown in the figure are evaluated for the temperature 300 K by using the Molière atomic potentials and averaging the individual particle-atom interactions over the bending period $\lambda_u = 400$ nm. The unit for the transverse coordinate in the plots is the inter-planar distance $d = 1.92$ \AA . The vertical lines mark the adjacent (110)-planes in the straight crystal.

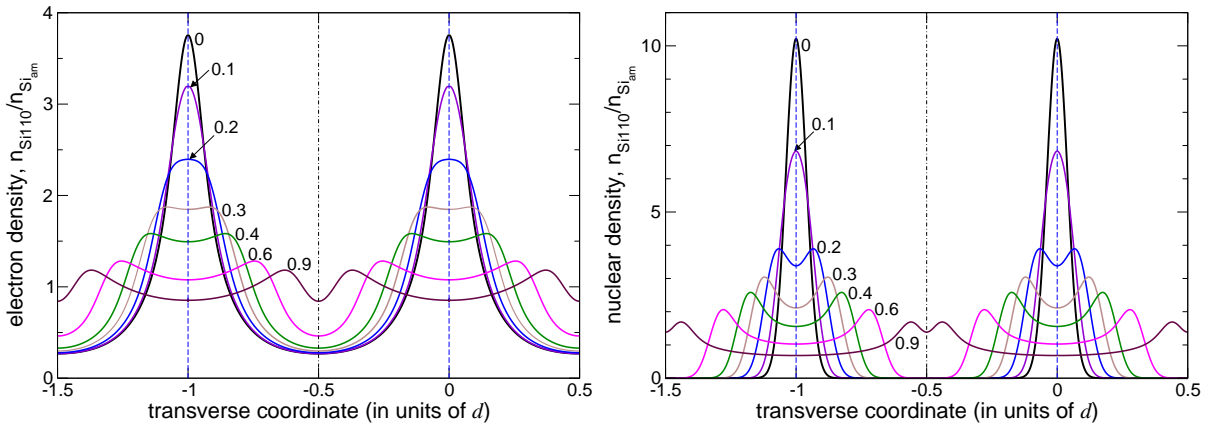


FIG. 4. Distributions of the electronic (left graph) and nuclear (right graph) densities along the transverse coordinate. The densities are normalized with respect to the values for amorphous silicon and correspond to the potentials shown in Fig. 3.

more dramatic way as the additional potential wells appear. These wells force the projectile to channel in spatial regions different from the channels for the straight and small-amplitude bent crystal. The latter regions are the “complementary” channels that appear in vicinities

of the centerlines for the periodically bent planes for the positrons, and are shifted away from the centerlines for the electrons. For the largest bending amplitude studied, $a = 0.9 \text{ \AA}$, the channeling can virtually be maintained only through the “complementary” channels. Thus, the potentials and charge densities shown in Figs. 3 and 4 elucidate evolution from “conventional” to “complementary” channeling of the projectiles with increasing the bending period.

The charge density distributions shown in Fig. 4 explain the peculiarities in the dependencies of the channeling lengths on the bending period. We reiterate that the densities are calculated within the same model as the continuous potentials studied in Fig. 3. The vertical lines in Fig. 4 mark the centerlines of the “conventional” channels for the electrons (dashed lines) and the positrons (chained lines). It is seen that, with increasing a both the electronic and nuclear crystalline densities gradually increase in the region between the two crystalline planes. As a result, motion of the positrons in the “conventional” channels is accompanied by increasing probability of collisions with the nuclei. This effect, together with lowering potential well, leads to a monotonous decrease of the channeling lengths. In contrast, in the “complementary” positron channels the densities decrease gradually, so that the corresponding channeling lengths increase. The non-monotonous variation with a of the lengths for “conventional” channeling of the electrons can be interpreted as follows. For small values of a , the decrease in the potential barrier out-powers the decrease in the densities in the central part of the channel. As a result, the channeling lengths initially decrease with increasing a . For $0.2 \leq a \lesssim 0.5 \dots 0.6 \text{ \AA}$, the density distributions become more diffuse with noticeably lower magnitudes in the center of the channel, making thereby the de-channeling process to develop more effectively. However, the inter-planar potential barrier still remains sufficiently high and supports the growth of $L_{p1,2}$ and L_{ch} with a . For the amplitudes larger than 0.6 \AA , the densities become comparable with those in the amorphous medium. Together with gradually decreasing potential barrier this yields decreasing channeling lengths.

Similar arguments referring to the continuous inter-planar potentials and charge densities, also explain the behavior of the electron and positron acceptances with varying bending amplitude. These argument readily confirm the particular outcome of the simulations that, for large amplitude values, $a \geq 0.6 \text{ \AA}$, the acceptances by the “complementary” channels become comparable or even larger than the acceptances by the “conventional” channels.

However, it remains to elucidate why the sum of the two acceptances can exceed the unity value, which might confuse one having in mind the meaning of acceptance as a *fraction* of the incident particles captured into the channeling mode at the entrance. The artifact values for the sum of “conventional” and “complementary” acceptances arise from double-counting of some particles as being accepted by both kinds of channels. Channeling in a SASP bent crystal develops with the trajectory oscillations of distinctly different periods, the long period λ_{ch} of channeling oscillations and the short period $\lambda_{\text{u}} \ll \lambda_{\text{ch}}$ of oscillations due to the bending. At the entrance, a particle experiencing the short-period oscillations is distinguished in the simulations as channeling regardless of the type, “conventional” or “complementary”. For illustration, we refer to the electron trajectory marked with the open circles in the right plot of Fig. 1. Near the crystalline entrance, this trajectory exhibits several oscillations with the period λ_{u} becoming thereby accepted by both the “conventional”, $-1.5 < y/d < -0.5$, and the “complementary”, $-1 < y/d < 0$, electron channels.

B. Radiation Spectra

The above described statistical studies on the channeling properties show the penetration lengths for the 855 MeV electrons to not exceed a value of about $12 \mu\text{m}$. We have therefore opted to study first the radiation for the $12 \mu\text{m}$ thick silicon crystal. The radiation spectra produced by the particles incoming along the (110) crystallographic planes are presented in Figs. 5 and 6. In Fig. 5, the spectra are studied for the fixed value of the bending period, $\lambda_{\text{u}} = 400 \text{ nm}$, and different values of the bending amplitudes in the range $a = 0 \dots 0.9 \text{ \AA}$. Fig. 6 presents the spectra produced for SASP bending with the amplitude $a = 0.4 \text{ \AA}$ and various periods $\lambda_{\text{u}} = 200 \dots 2500 \text{ nm}$. The sets of plots in both figures relate to the different projectiles, electrons and positrons (right and left plots, respectively), and different values for the radiation aperture, $\theta_{\text{max}} = 0.21 \text{ mrad}$ and $\theta_{\text{max}} = 4 \text{ mrad}$ (top and bottom, respectively). The smaller aperture value refers to a nearly forward emission from 855 MeV projectiles ($\theta_{\text{max}} \approx (3\gamma)^{-1}$) whereas the second value corresponds to the emission cone collecting almost all the radiation from the relativistic particles ($\theta_{\text{max}} \gg \gamma^{-1}$).

The spectra computed for the straight crystal and various bending amplitudes display a variety of features seen in Fig. 5. To be noticed are the pronounced peaks of the channeling radiation in the spectra for the straight crystal (the black solid-line curves). Nearly perfectly

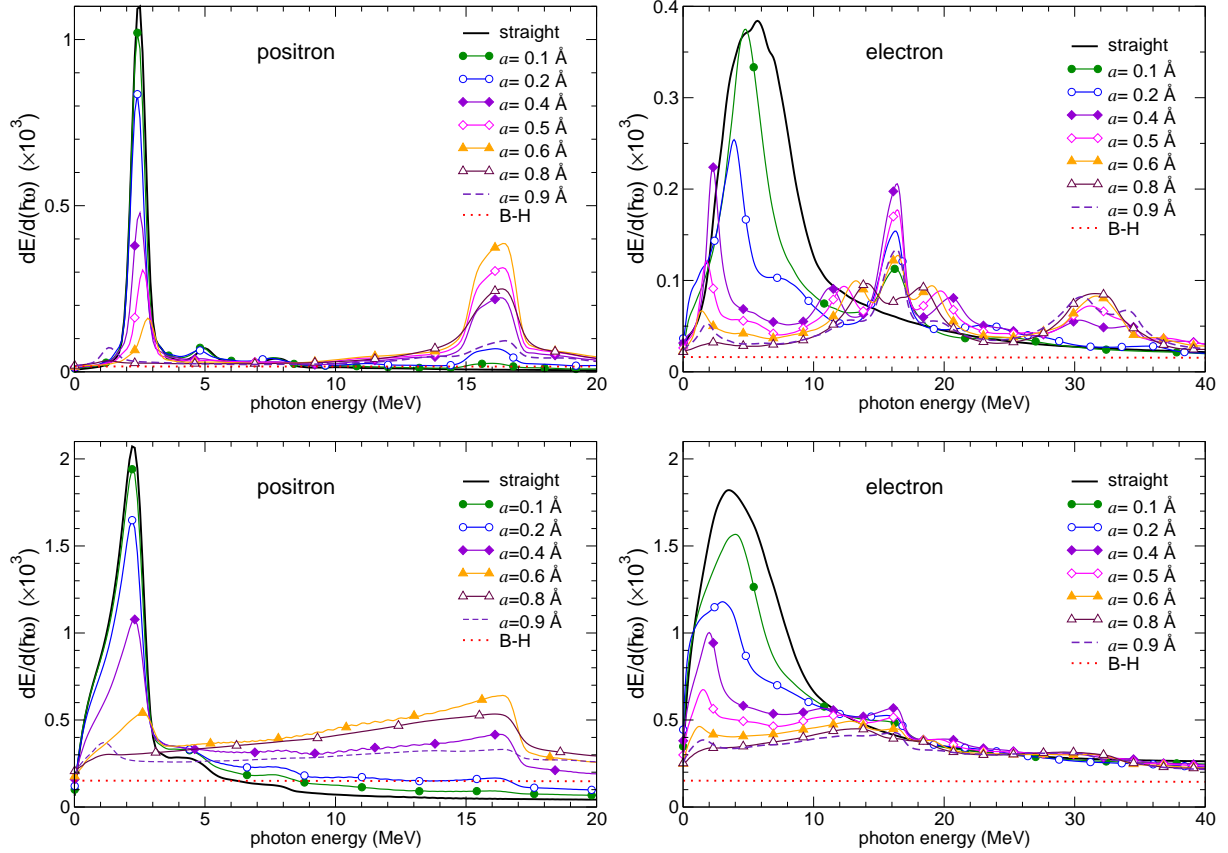


FIG. 5. Spectral distribution of radiation emitted by 855 MeV positrons (left) and electrons (right) in straight (thick solid lines) and SASP bent Si(110) with the period $\lambda_u = 400$ nm and various amplitudes a as indicated. Dotted lines mark the Bethe-Heitler spectra for amorphous silicon. The upper and lower plots correspond to the aperture values $\theta_{\max} = 0.21$ mrad and $\theta_{\max} = 4$ mrad, respectively. All spectra refer to the crystal thickness $L = 12$ micron.

harmonic channeling oscillations in the positron trajectories (the examples of the simulated trajectories can be found in [1, 12, 14]) lead to the undulator-type spectra of radiation with small values of the undulator parameter, $K < 1$ (see, e.g., [19]). The radiation spectra produced by the positrons in straight Si(110) clearly display the fundamental peaks of the channeling radiation at the emission energy ≈ 2.5 MeV, whereas the higher harmonics appear to be strongly suppressed according to the small values of K . In particular, for the smaller aperture value, $\theta_{\max} = 0.21$ mrad, the maximal spectral intensity in the fundamental peak is an order of magnitude larger than that for the second harmonics displayed by a small peak at about 5 MeV, and only a tiny hump of the third harmonics of channeling radiation can be recognized at about 7.5 MeV (see the top left plot in the figure). For the electrons

passing through the straight crystal, the channeling radiation peaks are less intensive and much broader than these for the positrons, as a result of stronger anharmonicity of the channeling oscillations in the trajectories. For the larger aperture value, $\theta_{\max} = 4$ mrad, a sizable part of the energy is radiated at the angles $\gamma^{-1} < \theta < \theta_{\max}$. For relatively large emission angles, the emission energy for the first channeling spectral harmonics decreases with increasing angle. As a result, the fundamental peaks of channeling radiation broaden and shift towards softer radiation energies.

The radiation spectra produced by the projectiles passing the SASP bent crystals display additional peaks, more pronounced for the smaller aperture value, which emerge from the short-period modulations of the projectile trajectories by the bent crystalline structure. The major novel feature of the radiation is that the peaks due the bending appear at the emission energies larger than the energies of the channeling peaks. For both types of the projectiles, the fundamental spectral peaks in the radiation emergent from SASP bending correspond to the emission energy about 16 MeV significantly exceeding the energy 2.5 MeV for the fundamental channeling spectral peaks. For the positrons, the peaks of radiation due to the bending are displayed in the spectra for the amplitude values 0.3...0.8 Å. For smaller values of a , the spectral peaks disappear because the positrons experience mainly “conventional” channeling staying away from the crystalline atoms and being therefore less affected by the SASP bent planes. In contrast, the electrons experience the impact of the bent crystalline structure at lower bending amplitudes. As seen in the right upper plot for the fundamental spectral peaks emergent from the bending, the peak for $a = 0.1$ Å is only two times lower than the maximal peak displayed for $a = 0.4$ Å.

To be noted are the spectral properties displayed for larger aperture value (bottom plots in Fig. 5). In the spectra produced by the electrons for the values of a exceeding 0.2 Å, noticeable are the lines at the energies around 32 MeV which are clearly the second harmonics of the radiation emergent from the SASP bending. The impact of increasing bending amplitude on the lines of channeling radiation for the electrons are decreasing line heights accompanied with line shifts towards the lower emission energies. In contrast, the positron spectra exhibit less peculiarities gradually converging to the Bethe-Heitler background with increasing radiation energies. Above 20 MeV, the radiation spectra for the positrons become fairly close to the background spectra and are not shown in the figure.

The impact of different periods of SASP bending on the radiation spectra is studied in

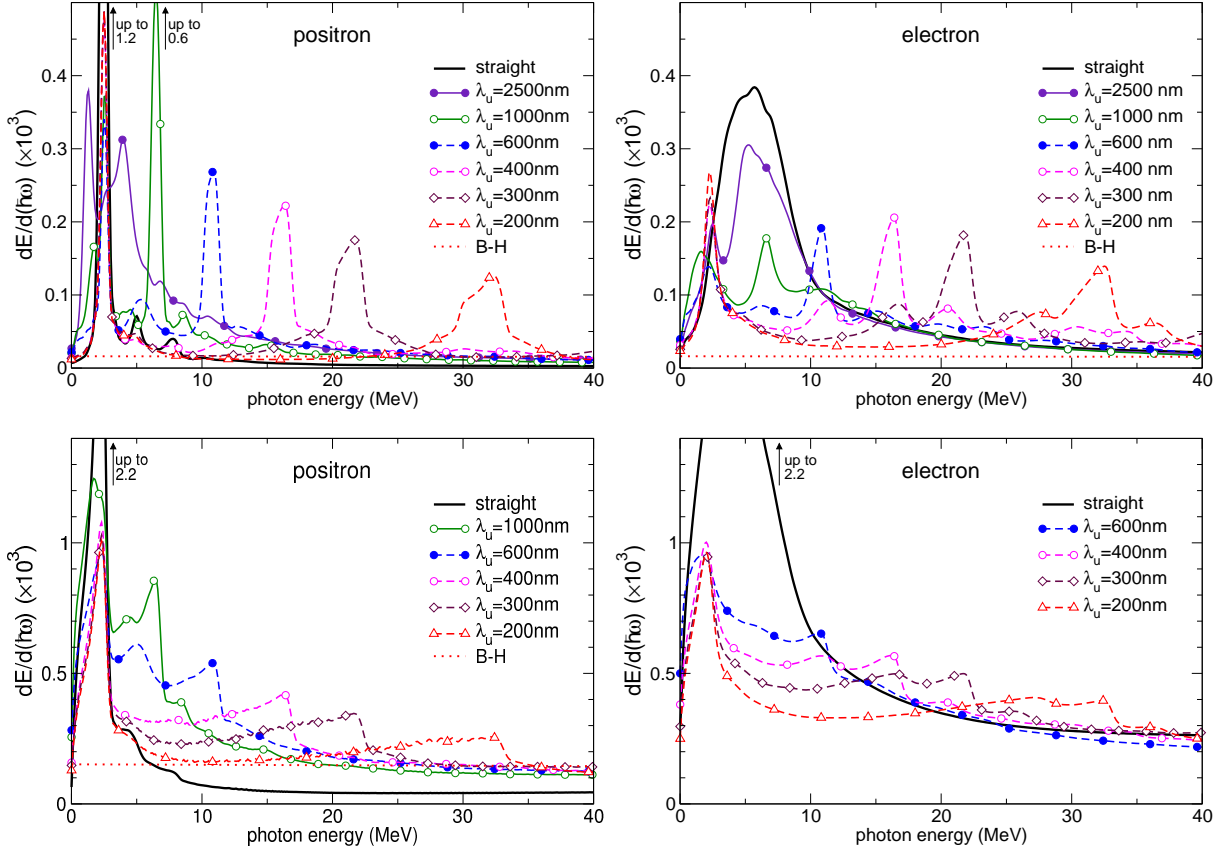


FIG. 6. Spectral distribution of radiation emitted by 855 MeV positrons (left) and electrons (right) in straight (thick solid curves) and SASP bent Si(110) with the bending amplitude $a = 0.4 \text{ \AA}$ and various periods λ_u as indicated. Dotted lines mark the Bethe-Heitler spectra for amorphous silicon. The spectra are computed for the crystal thickness $L = 12 \text{ }\mu\text{m}$, and two values for the radiation aperture, $\theta_{\text{max}} = 0.21 \text{ mrad}$ (upper plots) and $\theta_{\text{max}} = 4 \text{ mrad}$ (lower plots).

Fig. 6. The positions of the lines due to the bending are clearly seen to be in reciprocal relation with the bending period and shift towards hard-range radiation energies with decreasing λ_u . In contrast, the positions of channeling spectral lines, especially for the positrons, do not noticeably change with varying λ_u . Yet the shapes of the channeling lines are different for different bending amplitudes: the lines decrease in height as well as slightly shift towards the softer radiation energies with increasing bending period. The changes in the channeling radiation develop when the channeling lines and the lines resulting from the bending appear close to each other in the spectra and therefore interfere. The latter effects are more prominent for the larger aperture value (bottom plots in the figure), and in the spectra for the electrons (right plots) then in the spectra for the positrons (left plots).

To complete the studies on the radiation from SASP bent Si(110), we show in Fig. 7 the spectra simulated for four different thicknesses of the crystal, from 12 up to 150 micron. We can conclude that, the spectral shapes remain fairly the same with increasing crystalline thickness, with naturally increasing spectral intensities. The spectra in the figure also display the effects of varying bending amplitude. For both types of the projectiles, increasing the amplitude from 0.4 Å to 0.6 Å results in suppressing the channeling spectral lines and amplifying the lines produced due to the bending.

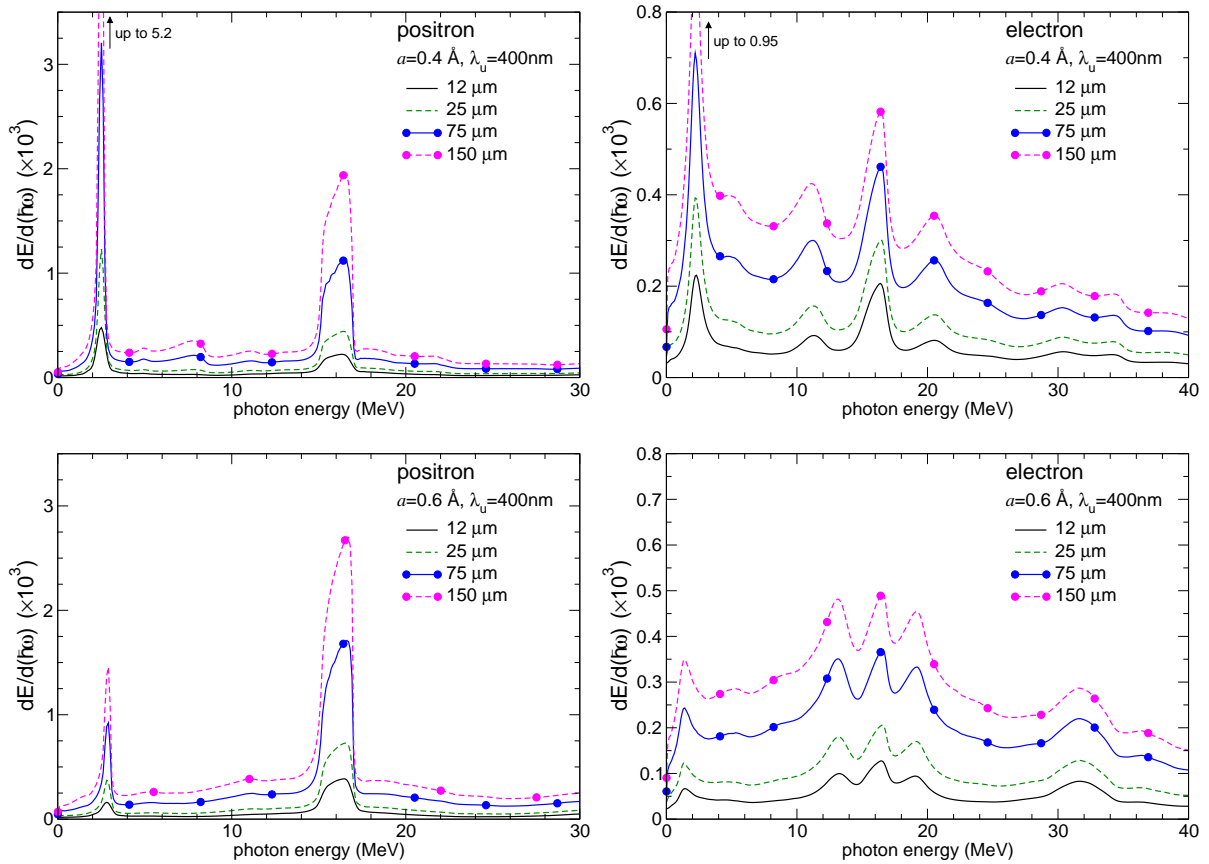


FIG. 7. Spectral distributions of radiation emitted by the 855 MeV electrons (right plots) and positrons (left plots) for SASP bending with the period $\lambda_u = 400$ nm and the amplitudes $a = 0.4$ Å (upper plots) and 0.6 Å (lower plots). The spectra are computed for the radiation aperture $\theta_{\max} = 0.21$ mrad and different crystal thicknesses indicated in the plots.

IV. CONCLUSIONS

In this paper, we have provided a systematic analysis of the channeling and radiation in short-period small-amplitude bent silicon crystals.

The statistical properties of channeling were described in terms of the lengths quantifying the spatial scales of de-channeling and re-channeling processes experienced by the projectiles. We have particularly focused on behavior of the lengths with varying the bending amplitude of the crystalline planes. With the amplitude increasing above already some moderate values, we have encountered a drastic change in the channeling process for the both types of projectiles. To elucidate the underlying physics, an analytical model has been developed in terms of the charge densities for the bent crystalline media which influence the particles moving through the crystal. The model reveals the channels optimal for “binding” the transverse motion of the projectiles to shift in the inter-planar direction with increasing the bending amplitude. The varying properties of channeling can be clarified in terms of two groups of the trajectories, the “conventional” and “complementary” ones. The supplementary analytical model of the continuous potential turns out to be helpful proving the simulations performed with MBN EXPLORER to be reliable, in particular, with respect to advance account for the interaction of the projectiles with individual atoms of the crystalline media.

ACKNOWLEDGMENTS

The work was supported by the European Commission (the PEARL Project within the H2020-MSCA-RISE-2015 call, GA 690991).

Appendix A: Continuous Potential in a SASP Bent Crystal

In this supplementary section we develop an approximation of continuous inter-planar potential. This potential and the corresponding distributions of the crystalline charge densities help in qualitative explanations of the results of numerical simulations on the motion and radiation for the electrons and positrons in SASP bent crystal, discussed above in Sects. III A and III B.

1. Continuous Potential of a Periodically Bent Plane

To derive the approximation of continuous potential in a crystal with periodically bent planes we use a general approach developed to study the radiation by fast projectiles in acoustically excited crystals (see, for example, Ref. [32]).

For the cosine periodic bending (1), the continuous potential \mathcal{U}_{pl} of a single plane can be presented in the form of a series:

$$\mathcal{U}_{\text{pl}}(a; y, z) = \mathcal{U}_0(a; y) + \sum_{m=1}^{\infty} \cos(2\pi mz/\lambda_u) \mathcal{U}_m(a; y) . \quad (\text{A1})$$

The expansion potentials $\mathcal{U}_m(a; y)$ can be related to the atomic potentials according to the expressions given in Ref. [32]. In the limit $a \rightarrow 0$ the expansion potentials with $n > 0$ vanish, $\mathcal{U}_m(0; y) = 0$, and the zero-order (non-periodic in z) term yields the continuous potential of the straight plane, $\mathcal{U}_{\text{pl}}(0; y, z) = \mathcal{U}_0(0; y) \equiv \mathcal{U}_{\text{pl}}(y)$. The later planar potential depends only on the transverse coordinate y . In the following, we assume the bending amplitude and period to satisfy the SASP bending condition

$$a < d \ll \lambda_u, \quad (\text{A2})$$

and relate the non-periodic term $\mathcal{U}_0(a; y)$ to the planar potential $\mathcal{U}_{\text{pl}}(y)$.

For a straight plane, the continuous potential is obtained by summing up the atomic potentials as exerted by the atoms distributed uniformly along the plane [2]. The surface density \mathcal{N} of the atoms is related to the volume density n as $\mathcal{N} = nd$, where d is the inter-planar spacing.

For the periodically bent plane we notice, that the atoms located within the interval $[y', y' + dy']$ with respect to the centerline $y' = 0$ are distributed along the planar surface with the density $2dl\mathcal{N}/\lambda_u$. By virtue of the strong inequality $a \ll \lambda_u$, Eq. (A2) above, we have $dl \approx dz$ and can approximate the planar atomic density as $2dz\mathcal{N}/\lambda_u$ (see Fig. 8). The continuous potential then can be calculated as follows

$$\begin{aligned} \mathcal{U}_0(a; y) &= \int_{-\lambda_u/4}^{\lambda_u/4} \frac{2dz}{\lambda_u} \mathcal{U}_{\text{pl}}(|y - a \cos(2\pi z/\lambda_u)|) \\ &= \frac{1}{\pi} \int_{-\pi/2}^{\pi/2} \mathcal{U}_{\text{pl}}(|y - a \cos \xi|) d\xi , \end{aligned} \quad (\text{A3})$$

where $\xi = 2\pi z/\lambda_u$, and appears to not depend on the bending period λ_u but be affected by the amplitude a . For $a = 0$ the potential reduces to potential $\mathcal{U}_{\text{pl}}(y)$ for the straight plane.

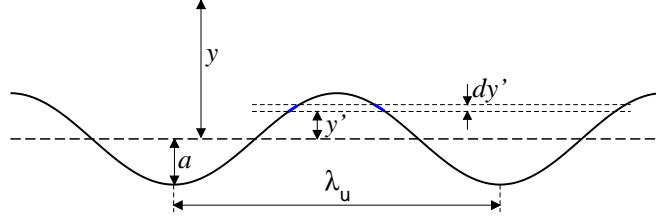


FIG. 8. Illustrative figure to the method of calculating the continuous potential for a periodically bent crystallographic plane (thick solid curve represents the bending profile (1)). See explanations in the text.

Similar procedure can be used to derive a non-periodic part of the distribution $n_0^{(+)}(a; y)$ of the nuclei in the periodically bent plane. One obtains

$$n_0^{(+)}(a; y) = \frac{1}{\pi} \int_{-\pi/2}^{\pi/2} n_{\text{pl}}^{(+)}(|y - a \cos \xi|) d\xi, \quad (\text{A4})$$

where $n_{\text{pl}}^{(+)}$ is the nuclear volume density for the straight plane. With account for the thermal vibrations, the latter density is given by the formula

$$n_{\text{pl}}^{(+)}(y) = \frac{n}{\sqrt{2\pi u_T^2}} \exp\left(-\frac{y^2}{2u_T^2}\right), \quad (\text{A5})$$

where u_T is the root-mean-square amplitude of the vibrations. The corresponding non-periodic part of distribution $n_0^{(-)}(a; y)$ of the crystalline electrons can be calculated from the Poisson equation as

$$n_0^{(-)}(a; y) = \frac{1}{4\pi e^2} \frac{d^2 \mathcal{U}_0(a; y)}{dy^2} + Z n_0^{(+)}(a; y), \quad (\text{A6})$$

where Z is the nucleus charge.

2. Continuous Inter-planar Potential

The non-periodic part $U_0(a; y)$ of the inter-planar potential is obtained by summing up the potentials (A3) of the separate planes. For the electrons it can be presented in the form

$$U_0(a; y) = \mathcal{U}_0(a; y) + \sum_{n=1}^{N_{\text{max}}} [\mathcal{U}_0(a; y + nd) + \mathcal{U}_0(a; y - nd)] + C, \quad (\text{A7})$$

where y is the transverse coordinate with respect to an arbitrary selected reference plane, and the sum describes a balanced contribution from the neighboring planes. Since the planar

potential (A3) falls off rapidly with increasing distance from the plane, Eq. (A7) provides a good approximation for the inter-planar potential at already moderate numbers of the terms included in the sum. In our calculations we use $N_{\max} = 2$. The constant term C can be varied to adjust $U_0(a; y = 0) = 0$. For the positrons, the inter-planar potential can be obtained from Eq. (A7) by reversing the signs of the planar potentials and selecting the constant C to adjust $U_0(a; y = \pm d/2) = 0$. Similar summation schemes allow to calculate the charge densities, nuclear and electronic, across the periodically bent channels.

3. The Molière Approximation

The integral in the right-hand side of Eq. (A3) for the continuous potential for a separate periodically bent plane can be evaluated using various model atomic potentials to quantify the potential $\mathcal{U}_{\text{pl}}(y)$ for a straight crystalline plane. A variety of model potentials can be found in, e.g., Refs. [2, 18, 19, 27, 33]. In our studies we use the Molière approximation for the atomic potentials [17] and evaluate the planar potential with accounting for the thermal vibrations of the atoms (cf. Eq. (A5)). This approach yields the planar potential in a closed analytical form [34, 35]

$$\mathcal{U}_{\text{pl}}(y) = 2\pi n_{\text{am}} d Z e^2 a_{\text{TF}} \sum_{i=1}^3 \left(F_i(y) + F_i(-y) \right) \quad (\text{A8})$$

with

$$F_i(\pm y) = \frac{\alpha_i}{2\beta_i} \exp\left(\frac{\beta_i^2 u_T^2}{2a_{\text{TF}}^2} \pm \frac{\beta_i y}{a_{\text{TF}}}\right) \operatorname{erfc}\left[\frac{1}{\sqrt{2}} \left(\frac{\beta_i u_T}{a_{\text{TF}}} \pm \frac{y}{u_T}\right)\right]. \quad (\text{A9})$$

In the above equations, n_{am} is the mean nuclear density in the amorphous medium, Z is charge number of the crystalline atoms, $a_{\text{TF}} = 0.8853 a_{\text{B}} Z^{-1/3}$ is the Thomas-Fermi radius ($a_{\text{B}} = 0.529 \text{ \AA}$ is the Bohr radius), $\alpha_{1,2,3} = (0.1, 0.55, 0.35)$ and $\beta_{1,2,3} = (6.0, 1.2, 0.3)$ are the parameters of the Molière approximation for the atomic potential. The complementary error functions, $\operatorname{erfc}(\zeta) = 2\pi^{-1/2} \int_{\zeta}^{\infty} \exp(-t^2) dt$, in Eq. (A9) result from averaging over the thermal vibrations of atomic nuclei.

The inter-planar potentials, presented in Fig. 3, were calculated from Eqs. (A3), (A7), (A8) and (A9). These potentials are also helpful in understanding the evolution of the lines of channeling radiation with varying bending period. To clarify this evolution we have investigated the periods λ_{ch} of the channeling oscillations in the trajectories and the

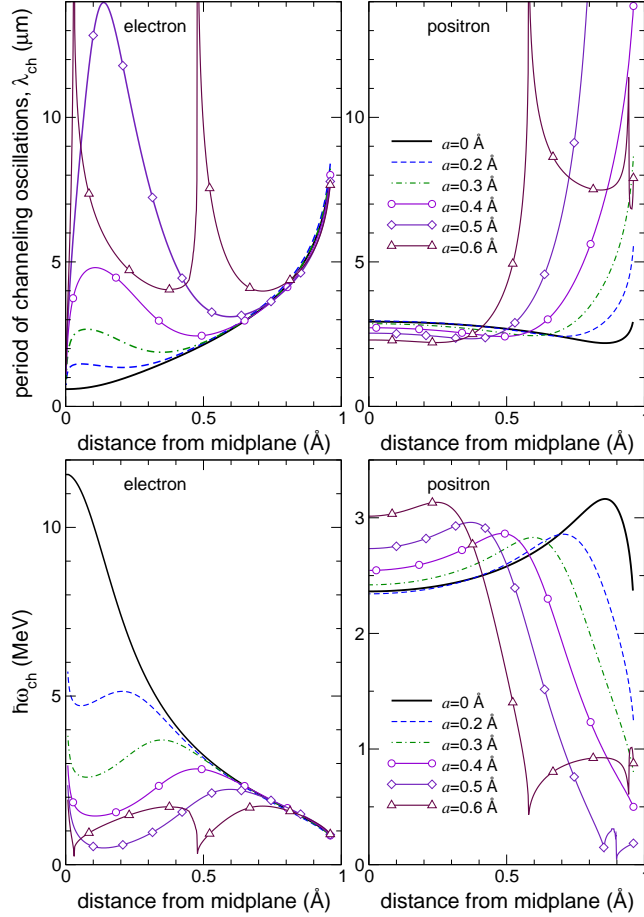


FIG. 9. Periods (upper plots) and energies (lower plots) of channeling oscillations for 855 MeV electrons (left panels) and positrons (right panels). The periods and energies are studied as functions of the distance from the channel centerlines for the continuous potentials shown in Fig. 3. The curves correspond to different bending amplitudes a as indicated ($a = 0$ corresponds to the straight crystal). See also explanations in the text.

corresponding radiation energies $\hbar\omega_{\text{ch}}$. These quantities have been evaluated as the functions of the amplitude of channeling trajectory oscillations. The amplitudes were fixed by the maximal transverse displacements of the projectiles from the channel centerlines, and the periods have been evaluated from the corresponding classical turning points and the shapes for the continuous inter-planar potential (see, e.g., Sec. C.2 in Ref. [1]). The channeling energies we deduced from the periods according to the relation $\omega_{\text{ch}} = 2\gamma^2(2\pi c/\lambda_{\text{ch}})$. The results for both types of the projectiles in the straight and bent with different amplitudes channels are shown in Fig. 9. For the straight crystals, the channeling radiation energies vary with the amplitude of the trajectory oscillations in a narrow energy range for the positrons

and in a prominently broader range for the electrons (see the lower plots in the figure). The latter properties correspond to the narrow channeling lines in the radiation spectra for the positrons, and the the broader lines in the spectra for the electrons, as seen in Fig. 5. With changing bending amplitude, the variation ranges of the radiation energy increase for the positrons and decrease for the electrons, and correspond to the evolution of the channeling lines in the simulated spectra.

REFERENCES

- [1] A.V. Korol, A.V. Solov'yov, Walter Greiner, *Channeling and Radiation in Periodically Bent Crystals*. Second edition (Springer-Verlag Berlin Heidelberg, 2014).
- [2] J. Lindhard, Influence of Crystal Lattice on Motion of Energetic Charged Particles, *K. Dan. Vidensk. Selsk. Mat. Fys. Medd.* **34**, 1–64 (1965).
- [3] A.V. Korol, A.V. Solov'yov, W. Greiner, Coherent Radiation of an Ultra-Relativistic Charged Particle Channeled in a Periodically Bent Crystal. *J. Phys. G* **24**, L45–L53 (1998).
- [4] A.V. Korol, A.V. Solov'yov, and W. Greiner, Photon Emission by an Ultra-Relativistic Charged Particle Channeling in a Periodically Bent Crystal, *Int. J. Mod. Phys. E* **8**, 49–100 (1999).
- [5] A. Kostyuk, Crystalline Undulator with a Small Amplitude and a Short Period, *Phys. Rev. Lett.* **110** 115503 (2013).
- [6] V.G. Bezchastnov, A.V. Korol, and A.V. Solov'yov, Radiation from Multi-GeV Electrons and Positrons in Periodically Bent Silicon Crystal, *J. Phys. B* **47**, 195401 (2014).
- [7] M.V. Medvedev, Theory of "Jitter" Radiation from Small-Scale Random Magnetic Fields and Prompt Emission from Gamma-Ray Burst Shocks, *The Astrophys. J.* **540**, 704–714 (2000).
- [8] S.R. Kellner, F.A. Aharonian, and D. Khangulyan, On the Jitter Radiation, *The Astrophys. J.* **774**, 61 (2013).
- [9] Tobias N. Wistisen, Kristoffer K. Andersen, Serdar Yilmaz, Rune Mikkelsen, John Lundsgaard Hansen, Ulrik I. Uggerhj, Werner Lauth, and Hartmut Backe, Experimental Realization of a New Type of Crystalline Undulator, *Phys. Rev. Lett.* **112**, 254801 (2014).

- [10] I.A. Solov'yov, A.V. Yakubovich, P.V. Nikolaev, I. Volkovets, and A.V. Solov'yov, Meso-BioNano Explorer - a Universal Program for Multiscale Computer Simulations of Complex Molecular Structure and Dynamics, *J. Comp. Chem.* **33**, 2412–2439 (2012).
- [11] <http://www.mbnexplorer.com/>
- [12] G.B. Sushko, V.G. Bezchastnov, I.A. Solov'yov, A.V. Korol, W. Greiner, and A.V. Solov'yov, Simulation of Ultra-Relativistic Electrons and Positrons Channeling in Crystals with MBN Explorer. *J. Comp. Phys.* **252**, 404–418 (2013).
- [13] G.B. Sushko, V.G. Bezchastnov, A.V. Korol, W. Greiner, A.V. Solov'yov, R.G. Polozkov, and V.K. Ivanov, Simulations of Electron Channeling in Bent Silicon Crystal, *J. Phys.: Conf. Ser.* **438**, 012019 (2013).
- [14] G.B. Sushko, A.V. Korol, W. Greiner, and A.V. Solov'yov, Sub-GeV Electron and Positron Channeling in Straight, Bent and Periodically Bent Silicon Crystals, *J. Phys.: Conf. Ser.* **438** 012018 (2013).
- [15] R.G. Polozkov, V.K. Ivanov, G.B. Sushko, A.V. Korol, and A.V. Solov'yov, Radiation Emission by Electrons Channeling in Bent Silicon Crystals. *Eur. Phys. J. D* **68** 268 (2014).
- [16] G.B. Sushko, A.V. Korol, and A.V. Solov'yov, Multi-GeV Electron and Positron Channeling in Bent Silicon Crystals, *Nucl. Instrum. Meth. B* **355**, 39–43 (2015).
- [17] G. Molière, Theorie der Streuung schneller geladener Teilchen I: Einzelstreuung am abgeschirmten Coulomb-Feld, *Z. f. Naturforsch. A* **2**, 133–145 (1947).
- [18] D.S. Gemmell, Channeling and Related Effects in the Motion of Charged Particles through Crystals. *Rev. Mod. Phys.* **46**, 129–227 (1974).
- [19] V.N. Baier, V.M. Katkov, and V.M. Strakhovenko, *Electromagnetic Processes at High On the Jitter Radiation Energies in Oriented Single Crystals* (World Scientific, Singapore, 1988).
- [20] U.I. Uggerhøj, *Ultrarelativistic particles in matter. Doctoral Dissertation* (Department of Physics and Astronomy, University of Aarhus, Denmark, 2011) (http://www.phys.au.dk/ulrik/Doct_dis_UIU.pdf).
- [21] H. Backe, P. Kunz, W. Lauth, and A. Rueda, Planar Channeling Experiments with Electrons at the 855-MeV Mainz Microtron. *Nucl. Instrum. Methods B* **266**, 3835–3851 (2008).
- [22] H. Backe, D. Krambrich, W. Lauth, J.L. Hansen, and U.K.I. Uggerhøj, X-ray Emission from a Crystal Undulator: Experimental Results at Channeling of Electrons, *Nuovo Cimento C* **34** 157–165 (2001).

- [23] H. Backe and W. Lauth, Private communication (2013).
- [24] L. Bandiera, E. Bagli, G. Germogli, V. Guidi, A. Mazzolari, H. Backe, W. Lauth, A. Berra, D. Lietti, M. Prest, D. De Salvador, E. Vallazza, and V. Tikhomirov, Investigation of the Electromagnetic Radiation Emitted by Sub-GeV Electrons in a Bent Crystal, *Phys. Rev. Lett.* **115**, 025504 (2015).
- [25] U. Wienands, T.W. Markiewicz, J. Nelson, R.J. Noble, J.L. Turner, U.I. Uggerhøj, T.N. Wistisen, E. Bagli, L. Bandiera, G. Germogli, V. Guidi, A. Mazzolari, R. Holtzapple, and M. Miller: Observation of Deflection of a Beam of Multi-GeV Electrons by a Thin Crystal, *Phys. Rev. Lett.* **114**, 074801 (2015).
- [26] A. Kostyuk, A.V. Korol, A.V. Solov'yov, and Walter Greiner, Planar Channeling of 855 MeV Electrons in Silicon: Monte Carlo Simulations, *J. Phys. B* **44**, 075208 (2011).
- [27] V.M. Biryukov, Yu.A. Chesnokov, and V.I. Kotov, *Crystal Channeling and its Application at High-Energy Accelerators*. (Springer-Verlag, Berlin, Heidelberg, 1996).
- [28] The concept of the exponential decay has been widely exploited to estimate the de-channeling lengths for various ultra-relativistic projectiles in the straight and bent crystals [21, 25, 29–31].
- [29] O.V. Bogdanov and S.N. Dabagov: Radiation Spectra of Channeled Electrons in Thick Si (111) Crystals, *J. Phys.: Conf. Ser.* **357**, 012029 (2012).
- [30] W. Scandale, R. Losito, E. Bagli, L. Bandiera, P. Dalpiaz, M. Fiorini, V. Guidi, A. Mazzolari, D. Vincenzi, G. Della Mea, E. Vallazza, A.G. Afonin, Yu.A. Chesnokov, V.A. Maishev, I.A. Yazynin, A.D. Kovalenko, A.M. Taratin, A.S. Denisov, Yu.A. Gavrikov, Yu.M. Ivanov, L.P. Lapina, V.V. Skorobogatov, D. Bolognini, S. Hasan, M. Prest, Measurement of the Dechanneling Length for High-Energy Negative Pions, *Phys. Lett.* **B719** 70–73 (2013).
- [31] A. Mazzolari, E. Bagli, L. Bandiera, V. Guidi, H. Backe, W. Lauth, V. Tikhomirov, A. Berra, D. Lietti, M. Prest, E. Vallazza, and D. De Salvador, Steering of a Sub-GeV Electron Beam through Planar Channeling Enhanced by Rechanneling, *Phys Rev Lett* **112** 135503 (2014).
- [32] G.V. Dedkov, Channeling Radiation in a Crystal Undergoing an Action of Ultrasonic or Electromagnetic Waves, *Phys. Stat. Sol. (b)* **184**, 535–542 (1994).
- [33] U.I. Uggerhøj, The interaction of relativistic particles with strong crystalline fields, *Rev. Mod. Phys.* **77**, 1131–1171 (2005).
- [34] B.R. Appleton, C., Erginsoy, and W.M. Gibson, Effects in the Energy Loss of 3-11-MeV Protons in Silicon and Germanium Single Crystals, *Phys. Rev.* **161**, 330–349 (1967)

- [35] C. Erginsoy, Anisotropic Effects in Interactions of Energetic Charged Particles in a Crystal Lattice, *Phys. Rev. Lett.* **15**, 360–363 (1965).